MULTISCALE MODEL. SIMUL.
Vol. 16, No. 3, pp. 1365–1391

THE STRUCTURE OF A DEWETTING RIM WITH STRONG SLIP: THE LONG-TIME EVOLUTION*

P. L. EVANS†, J. R. KING‡, AND A. MÜNCH§

Abstract. When a thin viscous film dewets from a solid substrate, the liquid forms a characteristic rim near the contact line as the contact line retracts. The shape of the rim and also the retraction rate vary strongly with the amount of slip that occurs at the liquid-solid substrate. If the slip length is very large compared to the thickness of the film, extensional stresses dominate the shear stresses, and the film evolution can be modeled by a thin-film model similar to the ones that occur in freely suspended films, with a correction from the viscous friction due to the large but finite slip. Asymptotic investigation of this model reveals that the rim has an amazingly rich asymptotic structure that moreover changes as the solution passes through four distinct time regimes. This paper continues previous work that focused on the first of these regimes [P. L. Evans, J. R. King, and A. Münch, *Appl. Math. Res. Express. AMRX*, 2006 (2006), 25262]. The structure of the solution is analyzed in detail via matched asymptotics and then the predictions for the contact line and profile evolution are compared with numerical results.

Key words. lubrication theory, strong slip, dewetting liquid film, matched asymptotics

AMS subject classifications. 34E05, 34E10, 34E15, 76D08, 76D45

DOI. 10.1137/15M1051221

1. Introduction.

When a liquid film is deposited on a solid substrate that is not perfectly wettable by the liquid, the formation of a hole (either by spinodal decomposition or nucleation) or a trench gives rise to a contact line that will typically retract, reducing the gas-liquid and liquid-solid interface areas in favor of the energetically preferable gas-solid interface. The liquid typically collects in a characteristic elevated capillary rim near the contact line. The shape of the rim profile and the retraction rates vary depending on both the bulk and the interface properties and have thus been the target of extended experimental and theoretical research. In these experiments, the films are typically very thin—in the micron or submicron range—and the observations of the profile and contact-line evolution can deliver important clues to the microscopic physics. This is particularly true for the role of real or apparent slip in microfluidics; see, for example, Lauga, Brenner, and Stone [23] for a review.

In macroscopic flows, no-slip conditions are usually assumed at the liquid-solid interface, but for thin, micron, and submicron polymer films, considerable apparent slip is possible and this has been used to explain the differences in the observed rim shapes and dewetting rates [31, 32]. In particular, for the no-slip situation, the contact-line position advances approximately linearly in time t, while in the presence of a large amount of slip as compared to the film thickness, it follows a $t^{2/3}$ power law. These laws have been derived using scaling arguments and have been compared

*Received by the editors December 3, 2015; accepted for publication (in revised form) July 8, 2018; published electronically September 25, 2018.
http://www.siam.org/journals/mms/16-3/M105122.html
†Helmholtz Centre Potsdam German Research Centre for Geosciences–GFZ, 14473 Potsdam, Germany (pevans@gfz-potsdam.de).
‡School of Mathematical Sciences, University of Nottingham, Nottingham NG7 2RD, UK (john.king@nottingham.ac.uk).
§Mathematical Institute, University of Oxford, Andrew Wiles Building, Oxford OX2 6GG, UK (muench@maths.ox.ac.uk).

with experiments [31, 32]. They can also be obtained from lubrication models which have different mobilities in the no-slip and the large slip case. The predicted retraction rates of the contact line are recovered from numerical solutions of these models as well as through approximations using matched asymptotics expansions [13, 21, 25, 27, 24]. Occasionally, the case of finite, nonzero slip has been considered as well [15, 24].

Systematic asymptotic approximation of the Stokes equations with a capillary interface and a Navier-slip condition at the liquid-solid interface reveals that beyond the large slip region considered previously, called the intermediate slip regime in [27], there is a distinguished limit for which extensional stresses enter the balance. This strong-slip limit leads to a system of partial differential equations (PDEs) [27, 16] instead of a scalar lubrication equation, similar to what appears in the modeling of free, suspended films [7] and extended to viscoelastic flow in [26]. A derivation in the context of poroviscous flows is given in [22] and in [12], which also contains gravity. A physical derivation of a model which includes the effect of extensional stresses but without explicit inclusion of surface tension can be found in [39].

The solutions of the strong-slip model behave quite differently compared to the models with less slip. Numerical solutions for the strong-slip model suggest that for large enough values of the slip parameter, the contact line first approaches a linear evolution in t before it tends to a 2/3-power-law behavior. Also, the cross section of the spatial profile decays monotonically to the unperturbed film, which is in marked contrast to the rims in the other models where the decay occurs through spatial oscillations (capillary ripples) [27, 36]. This explains suprising observations of monotone profiles made in experiments, which have been in fact exploited to determine slip lengths quantitatively [9, 10, 11, 1]. As the rim accumulates liquid and grows, the cross section changes from a very asymmetric to a more symmetric, rounded shape and eventually the oscillatory decay is recovered [27]. We remark that in addition to the differences observed for a retracting rim, the early stages of the onset of rupture via spinodal decomposition, as observed in the growth rates of the linear stability analysis of a flat, unstable film, are quite different [16, 30]. A rigorous investigation of the later stages of rupture in a strong-slip regime was carried out in [29, 28].

In this paper, we seek to understand the long-time evolution of the dewetting film for a strong-slip thin-film model in one dimension, so that the contact line is straight [2, 33]. This evolution is characterized by a rim of fluid increasing in thickness as it overruns the initial fluid film, taking up fluid from the latter. A careful asymptotic analysis and comparison with numerical results gives a comprehensive and detailed view of the intricate and complex evolution (through four major timescales and a continuum of intermediate timescales accompanied the appearance and merging of numerous spatial scales), which explains and complements observations from previous studies and quantifies the regimes in which different qualitative (oscillatory versus non-oscillatory, symmetric versus asymmetric) and power-law behaviors occur, aiding the interpretation of numerical and experimental results.

Given how innocuous the governing systems (2.1) appears, the asymptotic analysis is surprisingly involved and exemplifies features that are likely to be present in the treatment of other PDE systems, notably timescale separation involving only logarithmic differences between scales (see section 4.1) resulting from exponential dependence on space and a continuum of intermediate timescales (see section 5) associated with logarithmic dependence on time. Indeed, delicate exponential matching—here at the leading edge of the rim (see (4.14), (4.31))—can be crucial in governing the evolution. Specific other features of more general relevance in PDE theory include the appearance of both pseudoparabolic (mixed) and high-order derivatives, with (2.9) providing

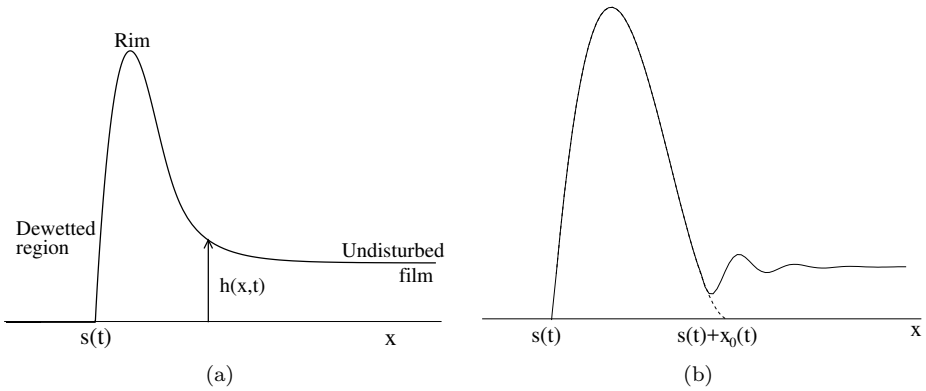

FIG. 1. *Schematics of the dewetting (retracting) rim.* (a) *Rim with monotone decay to the undisturbed film, typical for the earlier regimes.* (b) *Rim with an oscillatory decay, the transition to which happens on the fourth (and final) timescale, as described in the introduction and in section* 6 *(with a different asymptotic notation).*

the simplest such representation, and of nonlocal moving-boundary formulations—see (4.28) and (6.2); to emphasize this point, we record the first of the latter here without the distracting asymptotic notation required below, namely,

$$h\frac{\partial^2 h}{\partial x^2} - \frac{1}{2}\left(\frac{\partial h}{\partial x}\right)^2 = \dot{s}x - \frac{1}{2}, \qquad 0 < x < x_0(t), \tag{1.1}$$

$$h = 0 \qquad \text{at } x = 0 \text{ and } x_0(t), \tag{1.2}$$

$$\dot{s}(t) = \frac{1}{2(x_0(t)+2)}, \tag{1.3}$$

$$\int_0^{x_0(t)} h(x,t)\,dx = s(t). \tag{1.4}$$

This nonlinear boundary value problem (BVP) determines the fluid thickness $h(x,t)$ within the rim, the moving boundary $x_0(t)$, which measures the rim width (see Figure 1(b)), and, via the nonlocal (mass) constraint (1.4), the location $s(t)$ of the contact line separating wet and dry regions; via (1.3)–(1.4), $x_0(t)$ and $s(t)$ are coupled in a non-trivial way.

This study is the second part of earlier work by the same authors which covered the first timescale [8]. In section 2, we briefly recapitulate the formulation of the model and briefly state the main result from [8] for the contact-line evolution in the first timescale. The asymptotic investigation is carried out in sections 2 through 6, and comparisons with numerical solutions are carried out in section 8. Finally we summarize and conclude in section 9.

2. Formulation.

2.1. The initial boundary value problem. The model for a dewetting thin viscous film that we investigate here was considered by the same authors in [8], with a detailed derivation given in [27], so here we only recall the salient features. A schematic of the situation is shown in Figure 1.

Of primary interest is the evolution of the free surface which we describe by the film thickness $z = h(x,t)$, where x and z are the position along and normal to the substrate, respectively, and t denotes time. The flow in the film is governed by

the Navier–Stokes equations for a viscous incompressible liquid. The free surface is assumed to be subject to normal stresses due to capillarity but not to tangential stresses. At the substrate, we impose impermeability by setting the normal component to zero and a Navier-slip condition

$$U_{||} = B\frac{\partial U_{||}}{\partial z}$$

with a fixed slip length B for the tangential component $U_{||}$. We consider here the situation after a dewetted region has nucleated in the film, leading to the formation of a contact line at the position $x = s(t)$ in the lab frame, where the free surface meets the substrate at a given nonzero contact angle. The contact-line position is an unknown of the problem.

Using the thin-film approximation via expansions in terms of a small parameter related to the magnitude of the free surface slope, and neglecting inertia, one obtains the strong-slip model proposed by Münch, Wagner, and Witelski [27], Flitton [12], and Kargupta, Sharma, and Khanna [16],

$$\frac{\partial h}{\partial t} + \frac{\partial}{\partial x}(uh) = 0\,, \tag{2.1a}$$

$$4\frac{\partial}{\partial x}\left(h\frac{\partial u}{\partial x}\right) + h\frac{\partial^3 h}{\partial x^3} = \varepsilon(\dot{s} + u)\,, \tag{2.1b}$$

where u represents the depth averaged tangential velocity, in contrast to the u in the Navier-slip condition, which denotes the value of the tangential velocity at the substrate. These equations are supplemented by the boundary conditions

$$h = 0, \quad \frac{\partial h}{\partial x} = 1, \quad h\frac{\partial u}{\partial x} = 0, \quad u = 0 \quad \text{at } x = 0, \tag{2.2a}$$

$$h \to 1, \quad u \to -\dot{s} \quad \text{as } x \to \infty. \tag{2.2b}$$

Note that in (2.1), the model is formulated in a frame of reference that is moving with the contact line, so that $h = 0$ at a fixed position $x = 0$, but the unknown $\dot{s}$ remains in the problem via (2.1b) and (2.2b) instead. Moreover, h, x, and s have been scaled by h_∞, h_∞/λ, and h_∞/λ, respectively, where h_∞ is the thickness of the unperturbed film far away from the retracting rim and $\arctan\lambda$ is the contact angle. For the thin-film approximation to be uniformly valid, $\arctan\lambda$ is required to be small, so that in particular, we can use $\arctan\lambda \approx \lambda$. The velocity u and time t have been scaled by $\sigma\lambda/\mu$ and $\mu h_\infty/\sigma\lambda^2$, respectively, where σ and μ are the surface tension at the liquid-air interface and μ the dynamic viscosity of the liquid. The model leaves us with one parameter, $\varepsilon = h_\infty/B\lambda^2$, which we assume to be small, i.e., the slip length is very large, $B/h_\infty \gg 1/\lambda^2$. This was called the strong-slip regime in Münch, Wagner, and Witelski [27]. The model equations (2.1) represent dewetting in two dimensions, such as when nucleation has occurred along a straight edge, as in experiments by Reiter, Sferrazza, and Damman [33] and Bäumchen et al. [2].

As initial data for (2.1), we set

$$s(0) = 0 \quad \text{and} \quad h(x,0) = h_{\text{init}}(x) \quad \text{for } x \geq 0, \tag{2.3}$$

where, for definiteness in the numerical simulations,

$$h_{\text{init}}(x) = \begin{cases} 1 - (1 - x/2)^2 & \text{for } 0 \leq x \leq 2, \\ 1 & \text{for } 2 < x. \end{cases} \tag{2.4}$$

In general, it is sufficient if $h_{\rm init}(x)$ is smooth and positive for $x > 0$ and is consistent with the boundary conditions for h in (2.2). The long-time behavior was not found to depend significantly on the details of the initial profile $h_{\rm init}$, provided it makes the transition from $h_{\rm init}(x) = 0$ at the contact line to $h_{\rm init}(x) \approx 1$ over a region of width $\mathcal{O}(1)$. Notice that no separate initial condition is required for u.

Incidentally, reverting to the laboratory frame by setting $\dot{s} = 0$ in (2.1) we obtain

$$\frac{\partial}{\partial t}\left(\frac{1}{2}\left(\frac{\partial h}{\partial x}\right)^2\right) + \frac{\partial}{\partial x}\left(\frac{\partial h}{\partial x}\frac{\partial}{\partial x}(uh) - \frac{\partial^2 h}{\partial x^2}uh + 4u\frac{\partial}{\partial x}\left(h\frac{\partial u}{\partial x}\right)\right) = -4h\left(\frac{\partial u}{\partial x}\right)^2 - \varepsilon u^2 \tag{2.5}$$

as the equation governing the dissipation of the surface-energy density (kinetic energy being negligible in the current framework). The first term on the right-hand side of (2.5) represents viscous dissipation within the fluid, and the second that due to friction with the substrate.

2.2. Boundary condition counts. Various subproblems will (of course) arise in the asymptotic analysis and it will be important to ensure that each is correctly specified. Boundary condition counts play a key role in this regard and here we set out the relevant results for our full system (2.1)–(2.2), both to confirm that the formulation just described is correctly specified and to establish properties instructive for the analysis that follows. This system is of fourth order in x, one way to see this being to introduce the mass variable

$$m(x,t) = \int_0^x h(x',t)\,dx',$$

whereby

$$\frac{\partial m}{\partial t} + u\frac{\partial m}{\partial x} = 0, \tag{2.6}$$

allowing the system to be rewritten as a scalar equation, namely,

$$-4\frac{\partial}{\partial x}\left(\frac{\partial m}{\partial x}\frac{\partial}{\partial x}\left(\frac{\partial m}{\partial t}\Big/\frac{\partial m}{\partial x}\right)\right) + \frac{\partial m}{\partial x}\frac{\partial^4 m}{\partial x^4} = \varepsilon\left(\dot{s} - \frac{\partial m}{\partial t}\Big/\frac{\partial m}{\partial x}\right). \tag{2.7}$$

Because $s(t)$ is an unknown moving boundary, five boundary conditions are thus required in all. The local behavior of (2.1)–(2.2) as $x \to 0^+$ takes the form

$$h \sim x + \alpha(t)x^2\ln x + \beta t x^2, \qquad u \sim a(t)x^2\ln x + b(t)x^2,$$

with

$$\dot{\alpha} = -3a, \qquad \dot{\beta} = -a - 3b, \qquad 2\alpha = \varepsilon\dot{s},$$

so that

$$h \sim x - \frac{\varepsilon}{2}\dot{s}x^2\ln x + \beta x^2, \quad u \sim -\frac{\varepsilon}{6}\ddot{s}x^2\ln x + \frac{1}{3}\left(\frac{\varepsilon}{6}\ddot{s} - \dot{\beta}\right)x^2 \qquad \text{as } x \to 0^+, \tag{2.8}$$

containing arbitrary functions $\beta(t)$ and $s(t)$ as the only bona fide degrees of freedom. Because $s(t)$ arises in the PDEs rather than the local expansion per se, (2.8)

corresponds to three boundary conditions holding at $x = 0$, i.e., there is a single redundancy in (2.2a): indeed, (2.1a) and the first two of (2.2a) immediately imply the fourth of (2.2a).

As $x \to \infty$ we set

$$h \sim 1 + H, \qquad u \sim -\dot{s} + U$$

and linearize to obtain

$$\frac{\partial H}{\partial t} + \frac{\partial U}{\partial x} = 0, \qquad 4\frac{\partial^2 U}{\partial x^2} + \frac{\partial^3 H}{\partial x^3} = \varepsilon U,$$

giving the high-order pseudoparabolic equation

$$\varepsilon \frac{\partial H}{\partial t} = 4\frac{\partial^3 H}{\partial x^2 \partial t} - \frac{\partial^4 H}{\partial x^4}. \tag{2.9}$$

Applying the Liouville–Green (JWKB) method to determine the possible far-field behaviors of (2.9), where we stress that ε is to be viewed as $\mathcal{O}(1)$ for the current purposes, we find that there are two exponentially decaying degrees of freedom, i.e., the boundary condition count is as it should be. The first of these degrees of freedom appears as Φ is the far-field balance,

$$H \sim \frac{1}{t^{1/2}} \Phi\left(\frac{x}{t}\right) e^{-x^2/t} \qquad \text{as } x \to \infty, \tag{2.10}$$

whereby the right-hand side of (2.9) dominates, i.e., a heat-equation balance pertains. The second follows on neglecting the final term in (2.9), so that

$$\ln H \sim -\varepsilon^{1/2} x/2 \qquad \text{as } x \to \infty. \tag{2.11}$$

There is a subtlety in this second case: setting

$$H = \mathrm{e}^{-\varepsilon^{1/2} x/2} G$$

in (2.9) implies the far-field balance

$$\frac{\partial^2 G}{\partial x \partial t} \sim -\frac{\varepsilon^{3/2}}{64} G \tag{2.12}$$

so that (2.11) in fact subdivides into two:

$$H \sim \frac{1}{t^{1/2}} \mathrm{e}^{-\varepsilon^{1/2} x/2} \left(\Phi_+\left(\frac{x}{t}\right) \mathrm{e}^{i\varepsilon^{3/4}(xt)^{1/2}/4} + \Phi_-\left(\frac{x}{t}\right) \mathrm{e}^{-i\varepsilon^{3/4}(xt)^{1/2}/4} \right). \tag{2.13}$$

However, it is clear from the nature of the characteristics of the hyperbolic PDE (2.12) that although there are two degrees of freedom, Φ_+ and Φ_-, in (2.13), the accounting attributes only one to the far-field, the other being associated with the initial data.

3. Limit problems.

3.1. Quasi-steady behavior for negligible surface tension. Two limit cases of (2.1) recur in the asymptotic analysis that follows in section 4 and we therefore undertake their analysis in detail here in order not to break the flow of the subsequent asymptotic analysis; moreover, these subproblems (see (3.1) and (3.7)) both comprise ODEs and are potentially of interest in their own right. First, for sufficiently large x scalings, the time derivative in (2.1a) and the third derivative term in (2.1b) turn out

to be negligible in a number of the asymptotic regimes that arise below. In view of (2.2b), we then have

$$uh = -\dot{s}, \qquad 4\frac{\partial}{\partial x}\left(\frac{1}{h}\frac{\partial h}{\partial x}\right) = \varepsilon\left(1 - \frac{1}{h}\right). \tag{3.1}$$

Hence

$$\frac{1}{h^2}\left(\frac{\partial h}{\partial x}\right)^2 = \frac{\varepsilon}{2}\left(\ln h + \frac{1}{h} - 1\right), \tag{3.2}$$

i.e., (3.1) can be solved fully in terms of a single quadrature. Corresponding to $\varepsilon^{1/2}(x_0 - x) \gg 1$ in (3.3), the $1/h$ term in (3.2) is negligible, and retaining all the remaining terms implies

$$h \sim \mathrm{e}^{1+\varepsilon(x_0-x)^2/8}, \qquad u \sim -\dot{s}\mathrm{e}^{\left(1+\varepsilon(x_0-x)^2/8\right)}, \tag{3.3}$$

for arbitrary $x_0(t)$; these balances will play an important role in the matching—see (4.14) and (4.31) below.

To clarify the status of this asymptotic balance, we set

$$x = \varepsilon^{-1/2}y, \quad h = \eta/\delta$$

with $0 < \delta \ll 1$ so that (3.2) becomes

$$\frac{\partial \eta}{\partial y} = -2^{-1/2}\eta\left(\ln(1/\delta) + \ln\eta - 1 + \delta/\eta\right)^{1/2},$$

which we will analyze systematically in the limit $\delta \to 0$, wherein a continuum of scales arises: to all powers of $\ln(1/\delta)$, the final term can be neglected for $\eta = \mathcal{O}(\delta^\gamma)$ for any $\gamma < 1$, in which case

$$\eta \sim \delta\mathrm{e}^{1+(Y_0-y)^2/8}, \tag{3.4}$$

as in (3.3), applies for some $Y_0(t) = \varepsilon^{1/2}x_0(t)$, i.e., (3.4) captures the asymptotic behavior of (3.2) over the continuum of scales

$$\eta = \mathcal{O}(\delta^\gamma), \quad Y_0 - y = \mathcal{O}(\nu\ln^{\frac{1}{2}}(1/\delta)),$$

where $\nu = (8(1-\gamma))^{1/2} > 0$. This of course requires $y < Y_0$ and breaks down for ξ, $h = \mathcal{O}(1)$, where $y = Y_0 + \xi$, giving the full balance

$$\frac{dh}{d\xi} = -2^{-1/2}h\left(\ln h + \frac{1}{h} - 1\right)^{1/2} \qquad \text{as } \xi \to -\infty \qquad h \sim \mathrm{e}^{1+\xi^2/8}, \tag{3.5}$$

in (3.2), implying that

$$\frac{dh}{d\xi} \sim -\frac{1}{2}(h-1)$$

as $h \to 1^+$, so that

$$h \sim Ae^{-\xi/2} \qquad \text{as } \xi \to +\infty, \tag{3.6}$$

where the constant A can be determined from (3.5), which is solvable as a quadrature. There is then a transition to (2.13) that can be described by a Liouville–Green approach.

3.2. Quasi-steady behavior for negligible substrate friction. The second limit case worth covering at this stage involves again neglecting the time derivative in (2.1a), but now also disregarding of the right-hand side of (2.1b), giving

$$uh = -\dot{s}, \qquad 4\dot{s}\frac{1}{h}\frac{\partial h}{\partial z} + h\frac{\partial^2 h}{\partial z^2} - \frac{1}{2}\left(\frac{\partial h}{\partial z}\right)^2 = -\frac{1}{2}\Lambda^2(t), \tag{3.7}$$

wherein z is a (time-dependent) translate of x that will in what follows be determined by matching and the boundary conditions (2.2) do not in general apply, so in particular, $\Lambda \equiv 1$ need not hold. This reduction plays a key role below: see the remark following (4.23) and the leading-order solution given by (4.30); the role of $\Lambda(t)$ as a mesoscopic contact angle is apparent from the latter in particular. The relevant boundary conditions for the ODE in (3.7) that will be of interest are

$$h = \Lambda(t)(-z) \quad \text{as } z \to -\infty, \qquad h \to 0 \quad \text{as } z \to +\infty. \tag{3.8}$$

Setting

$$h(z,t) = 4\dot{s}G(\xi)/\Lambda(t), \qquad u(z,t) = -\Lambda(t)/4G(\xi), \qquad \xi = \Lambda^2(t)z/4\dot{s} \tag{3.9}$$

allows $\dot{s}$ and Λ to be scaled out, leaving the parameter-free initial value problem

$$\begin{gathered} G\frac{d^2G}{d\xi^2} - \frac{1}{2}\left(\frac{dG}{d\xi}\right)^2 + \frac{1}{G}\frac{dG}{d\xi} = -\frac{1}{2}, \\ G = -\xi \quad \text{as } \xi \to -\infty, \end{gathered} \tag{3.10}$$

which determines G up to translations of ξ. It follows from (3.10) that

$$G \sim B\mathrm{e}^{-\xi/2} \qquad \text{as } \xi \to +\infty \tag{3.11}$$

for some positive constant B that can be set to unity by choice of the origin of ξ, though to determine this choice of origin in what follows would require higher-order matching, which we shall not undertake. This BVP determines $\bar{g}$ both in (4.22) and in (4.30) below.

4. Asymptotic analysis.

4.1. The first timescale and a subsequent rescaling. In the following, we focus on understanding the evolution of the rim for small $\varepsilon \ll 1$. It turns out that there are several distinguished limits. The first timescale, for moderate ("early") times, $t = \mathcal{O}(1)$, was the focus of the earlier paper by Evans, King, and Münch [8], so we only give a brief summary here. In this limit, the asymptotic structure comprises two regions, namely, an inner region, close to the contact line, and an outer region. For $t \to \infty$, the inner solution takes on a self-similar form, while the outer solution subdivides into three regions. Until the inner merges with the adjacent outer subregion, which signals the distinguished limit that defines the second timescale, the evolution of the contact line $s(t) = \varepsilon^{-1/2}S(t;\varepsilon)$ is given by $S(t;\varepsilon) = S_0(t) + o(1)$, with

$$S_0 \sim \frac{t}{4\sqrt{2}\ln^{1/2} t} \qquad \text{for } t \to \infty. \tag{4.1}$$

For later reference, we record here that in [8], this expression was derived as an asymptotic solution of

$$\dot{S}_0 = \frac{1}{4\sqrt{2}}\left(\ln\left(\frac{t}{8}\right) - 1\right)^{-1/2} \tag{4.2}$$

for $t \to \infty$.

The next two timescales differ from each other only by scalings logarithmic in ε. In terms of powers of ε, the appropriate initial rescalings are

$$t = \varepsilon^{-1/2}\tau, \quad x = \varepsilon^{-1/2}y, \quad h = \varepsilon^{-1/2}g, \quad s(t) = \varepsilon^{-1}\sigma(\tau), \tag{4.3}$$

which give

$$\frac{\partial g}{\partial \tau} + \frac{\partial}{\partial y}(gu) = 0, \tag{4.4a}$$

$$4\frac{\partial}{\partial y}\left(g\frac{\partial u}{\partial y}\right) + g\frac{\partial^3 g}{\partial y^3} = \dot{\sigma} + \varepsilon^{1/2}u, \tag{4.4b}$$

where the dot henceforth denotes differentiation with respect to the relevant timescale—here τ. Thus, to all orders in $1/\mu(\varepsilon)$, where

$$\mu \equiv \ln^{1/2}(1/\varepsilon),$$

the inner equations will be given by (4.4a) and a suitable limit of

$$4g\frac{\partial u}{\partial y} + g\frac{\partial^2 g}{\partial y^2} - \frac{1}{2}\left(\frac{\partial g}{\partial y}\right)^2 = \dot{\sigma}y - \frac{1}{2}. \tag{4.5}$$

In both cases, the behavior in the outer regions is captured by the balance in section 3.1.

4.2. The second timescale. Guided by the need to match into the first timescale, here we set

$$\tau = \frac{1}{\mu}\bar{\tau}, \quad y = \frac{1}{\mu}\bar{y}, \quad g = \frac{1}{\mu}\bar{g}, \quad \sigma(\tau) = \frac{1}{\mu^2}\bar{\sigma}(\tau). \tag{4.6}$$

The $\dot{\sigma}$ term in (4.5) is a factor $1/\mu^2$ smaller than the other terms, giving the leading-order balance

$$\frac{\partial \bar{g}}{\partial \bar{\tau}} + \frac{\partial}{\partial \bar{y}}(\bar{g}u) = 0, \tag{4.7a}$$

$$4\bar{g}\frac{\partial u}{\partial \bar{y}} + \bar{g}\frac{\partial^2 \bar{g}}{\partial \bar{y}^2} - \frac{1}{2}\left(\frac{\partial \bar{g}}{\partial \bar{y}}\right)^2 = -\frac{1}{2}, \tag{4.7b}$$

with

$$\bar{g} = 0, \quad u = 0 \quad \text{at } \bar{y} = 0, \qquad \bar{g} = 0 \quad \text{at } \bar{\tau} = 0. \tag{4.8}$$

The asymptotic reduction (4.7a)–(4.7b) is precisely the one that can be reformulated as the reaction-diffusion equation (B.5) in the appendix.

The appropriate next step is to undertake a degree-of-freedom count on (4.7). As $y \to 0$, we have

$$g \sim y + \gamma(\bar{\tau})y^2, \qquad u \sim \frac{1}{3}\dot{\gamma}(\bar{\tau})y^2,$$

containing a single degreee of freedom $\gamma(\bar{\tau})$. As $\bar{y} \to \infty$, (4.7a) implies

$$\bar{g}u \to -\bar{J}(\bar{\tau}) \qquad \text{as } \bar{y} \to \infty, \tag{4.9}$$

where $\bar{\tau}$ remains to be determined. Equation (4.7b) then gives

$$\bar{g} \sim \bar{B}(\bar{\tau})\, \mathrm{e}^{-\bar{y}/8\bar{J}} \qquad \text{as } \bar{y} \to \infty. \tag{4.10}$$

Finally, a further degree of freedom arises from the highest derivative term in (4.7b): setting

$$\bar{g} \sim \bar{B}(\bar{\tau})\mathrm{e}^{-\bar{y}/8\bar{J}} + \cdots + \bar{G} \qquad \text{as } \bar{y} \to \infty \tag{4.11}$$

and linearizing implies

$$\frac{4\bar{J}}{\bar{B}}\frac{\partial}{\partial \bar{y}}\left(\mathrm{e}^{\bar{y}/8\bar{J}}\bar{G}\right) + \bar{B}\mathrm{e}^{-\bar{y}/8\bar{J}}\left(\frac{\partial^2 \bar{G}}{\partial \bar{y}^2} + \frac{1}{8\bar{J}}\frac{\partial \bar{G}}{\partial \bar{y}} + \frac{1}{64\bar{J}^2}\bar{G}\right) = 0,$$

where the ellipsis in (4.11) is required because $\bar{G}$ proves exponentially smaller than the leading term therein. Applying the Liouville–Green (JWKB) method then yields

$$\bar{G} \sim \bar{C}(\bar{\tau}) \exp\left(-\frac{16\bar{J}^2}{\bar{B}^2}\exp\left(\bar{y}/4\bar{J}\right) - \bar{y}/4\bar{J}\right) \qquad \text{as } \bar{y} \to \infty. \tag{4.12}$$

Thus there are three (i.e., the maximal possible number) degrees of freedom, namely, $\bar{J}$, $\bar{B}$, and $\bar{C}$ in (4.9), (4.10), and (4.12), in the far-field behavior of (4.7)–(4.8) and its correct specification requires matching with outer regions, these being as analyzed in section 3.1. Under the current scalings, the first of (3.1) implies immediately that

$$\dot{\bar{\sigma}}(\bar{\tau}) = \bar{J}(\bar{\tau}) \tag{4.13}$$

in (4.9). However, $\bar{\sigma}$ is itself unknown and (4.13) should be viewed as the equation that determines it from $\bar{J}$, rather than vice versa.

Next, setting $x_0 = \varepsilon^{-1/2}\mu\bar{Y}_0(\varepsilon)$ in the first of (3.3)—which is in keeping with the validity of (3.3) requiring that $\varepsilon^{1/2}(x_0 - x) \gg 1$—leads on matching with (4.10) to

$$\bar{B}\mathrm{e}^{-\bar{y}/8\bar{J}} \sim \mu\varepsilon^{1/2} e^{1+\mu^2\bar{Y}_0^2/8-\bar{Y}_0\bar{y}/4}, \tag{4.14}$$

so that the algebraic dependence on ε requires that $\bar{Y}_0 \sim 2$, and equating the final terms on the left and right then yields $\bar{J}$, and hence, by (4.13), $\bar{\sigma}$,

$$\bar{J} \sim \frac{1}{4}, \qquad \bar{\sigma} \sim \frac{\bar{\tau}}{4}, \tag{4.15}$$

the latter matching with (4.1). Thus (4.7)–(4.8) are supplemented by the condition

$$\bar{g}u \to -\frac{1}{4} \qquad \text{as } \bar{y} \to \infty \tag{4.16}$$

to give a correctly specified initial BVP (IBVP), $\bar{\sigma}$ being determined in (4.15) without requiring this IBVP to be solved. We note using (4.16) that it follows from (4.7a) and (4.8) that

$$\int_0^\infty \bar{g}(\bar{y}, \bar{\tau})d\bar{y} = \frac{\bar{\tau}}{4}. \tag{4.17}$$

We emphasize that (4.16) can be inferred only through the above matching to (3.3), which is associated with the transition to the initial film thickness $h = 1$: in no sense is it implicit in (4.7)–(4.8), and it is the only way substrate friction enters the leading-order problem on this timescale, it being absent from (4.7)–(4.8). We now analyze (4.7)–(4.8) subject to (4.16) as $\bar{\tau} \to 0$ and as $\bar{\tau} \to +\infty$, the latter in preparation for the analysis of the next timescale and the former to confirm matching with the results of [8].

Small $\bar{\tau}$. As $\bar{\tau} \to 0$ we have the separable behavior

$$\bar{g} \sim \bar{\tau} G(\bar{y}), \qquad u \sim \frac{1}{\bar{\tau}} U(\bar{y}),$$

whereby the dominant balance in (4.7) becomes

$$G + \frac{d}{d\bar{y}}(GU) = 0, \qquad 4G\frac{dU}{d\bar{y}} = -\frac{1}{2}, \tag{4.18}$$

and hence, using (4.16),

$$G = \frac{1}{8} e^{-\bar{y}/2}, \qquad U = -2\left(e^{\bar{y}/2} - 1\right), \tag{4.19}$$

so that in (4.11)

$$\bar{B}(\bar{\tau}) \sim \frac{1}{8}\bar{\tau} \qquad \text{as } \bar{\tau} \to 0^+.$$

Equation (4.18) disregards the highest derivative in (4.7b), necessitating a boundary layer in which the similarity reduction,

$$\bar{g} \sim \bar{\tau}\bar{G}(\bar{\xi}), \qquad u \sim \bar{U}(\bar{\xi}), \qquad \bar{\xi} = \bar{y}/\bar{\tau},$$

which represent a full balance in (4.7), pertains; the boundary and matching conditions read

$$\bar{G} = \bar{U} = 0 \quad \text{at } \bar{\xi} = 0, \qquad \bar{G} \sim \frac{1}{8}, \ \bar{U} \sim -\bar{\xi} \quad \text{as } \bar{\xi} \to +\infty.$$

Large $\bar{\tau}$. The large $\bar{\tau}$ limit also subdivides into two, an inner region discussed below and an outer one containing most of the mass (4.17), with $\bar{y}$, $\bar{g} = \mathcal{O}(\bar{\tau}^{1/2})$, $u = \mathcal{O}(\bar{\tau}^{-1/2})$, whereby the first term in (4.7b) is the only negligible one in (4.7). This implies

$$\bar{g} \sim \bar{y}\left(1 - \bar{y}/\bar{y}_0\right)_+, \qquad \bar{y}_0 \sim K\bar{\tau}^{1/2} \qquad \text{as } \bar{\tau} \to \infty \tag{4.20}$$

for some constant K that is determined below, and hence by (4.7a)

$$u \sim -\dot{\bar{y}}_0 \bar{y}^2 \,/ 3\bar{y}_0^2(1 - \bar{y}/\bar{y}_0) \qquad \text{as } \bar{\tau} \to \infty. \tag{4.21}$$

Here, $\bar{y}_0$ corresponds to the width of a growing rim of fluid in which h is much larger than the initial layer depth; this quantity will play an important role henceforth. It is noteworthy that the rim profile (4.20) for $\bar{\tau} \gg 1$ is parabolic (and hence, in particular, symmetric), as it is for large times in the no-slip and weak slip regime [13, 31].

In the inner region $\bar{\xi} = \mathcal{O}(1)$, where $\bar{y} = \bar{y}_0(\bar{\tau}) + \bar{\xi}$, the scalings on the dependent variables are simply $\bar{g} = \mathcal{O}(1)$, $u = \mathcal{O}(1)$, with u given in terms of $\bar{g}$ by

$$\bar{g}u \sim -1/4, \tag{4.22}$$

and matching with (4.20)–(4.21) for $\bar{y} \sim \bar{y}_0$ requires

$$\bar{y}_0\dot{\bar{y}}_0/3 = 1/4,$$

so that

$$K = \sqrt{\frac{3}{2}} \tag{4.23}$$

in (4.20). Furthermore $\bar{g} \sim G(\bar{\xi})$, where G is given by the BVP (3.10), but with a higher-order calculation being required to determine the ξ translate referred to there, and hence B in (3.11). Given $G(\xi)$, u can be then be obtained from (4.22), with

$$\bar{B}(\bar{\tau}) \sim B\mathrm{e}^{\bar{y}_0(\tau)/2} \qquad \text{as } \bar{\tau} \to \infty \tag{4.24}$$

holding in (4.10), B being as in (3.11).

Two final comments are in order here. First, it will prove instructive to note that equating the two sides of (4.14) exactly (rather than asymptotically for small ε and hence large μ, this being the limit in which the balance has been derived) gives

$$\bar{Y}_0 = 2\left(1 + 2\frac{\ln(\bar{B}/\mu) - 1}{\mu^2}\right)^{1/2}, \qquad \bar{J} = 1/2\bar{Y}_0, \tag{4.25}$$

so the above analysis will break down when $\bar{B}$ becomes sufficiently large with respect to μ, leading on to the third timescale. Second, for the record we note that the corresponding IBVP for the reduced order problem (B.5) in the appendix has that (B.5) holds for $0 < m < t/4$ (cf. (4.17)) with (here we revert to the original notation)

$$\omega \sim (2m)^{-3/4} \qquad \text{as } m \to 0^+, \qquad \omega \sim \left(\frac{1}{2}\left(\frac{t}{4} - m\right)\right)^{-3/2} \qquad \text{as } m \to \frac{t^-}{4},$$

i.e., one has singular boundary data on the reaction-diffusion equation.

4.3. The third timescale. Because $\bar{y}$ scales with $\bar{\tau}^{1/2}$ in (4.20), the neglected $\dot{\sigma}$ term from (4.5) ceases to be negligible when $\bar{\tau} = \mathcal{O}(\mu^4)$. We accordingly set

$$\tau = \mu^3\hat{\tau}, \quad y = \mu\hat{y}, \quad g = \mu\hat{g}, \quad u = \hat{u}/\mu^2, \quad \sigma(\tau) = \mu^2\hat{\sigma}(\hat{\tau}), \tag{4.26}$$

to give

$$\frac{\partial \hat{g}}{\partial \hat{\tau}} + \frac{\partial}{\partial \hat{y}}(\hat{g}\hat{u}) = 0, \tag{4.27a}$$

$$\frac{4}{\mu^2}\hat{g}\frac{\partial \hat{u}}{\partial \hat{y}} + \hat{g}\frac{\partial^2 \hat{g}}{\partial \hat{y}^2} - \frac{1}{2}\left(\frac{\partial \hat{g}}{\partial \hat{y}}\right)^2 = \dot{\hat{\sigma}}\hat{y} - \frac{1}{2}. \tag{4.27b}$$

Thus in the outer region $\hat{y} = \mathcal{O}(1)$, $0 < \hat{y} < \hat{y}_0(\hat{\tau})$, we have (4.27a), and, at leading order,

$$\hat{g}\frac{\partial^2 \hat{g}}{\partial \hat{y}^2} - \frac{1}{2}\left(\frac{\partial \hat{g}}{\partial \hat{y}}\right)^2 = \dot{\hat{\sigma}}\hat{y} - \frac{1}{2}. \tag{4.28}$$

Before completing the specification of this outer problem, we must turn to the inner one, whereby

$$\hat{y} = \hat{y}_0(\hat{\tau}) + \hat{\xi}/\mu^2 \tag{4.29}$$

with $\hat{\xi}$, $\bar{g}$, $u = \mathcal{O}(1)$ and at leading order

$$\bar{g}u = -\dot{\hat{\sigma}}, \qquad 4\bar{g}\frac{\partial u}{\partial \hat{\xi}} + \bar{g}\frac{\partial^2 \bar{g}}{\partial \hat{\xi}^2} - \frac{1}{2}\left(\frac{\partial \bar{g}}{\partial \hat{\xi}}\right)^2 = \dot{\hat{\sigma}}\hat{y}_0 - \frac{1}{2}.$$

Hence we can again appeal to the analysis of section 3.2 to infer that

$$\bar{g}(\hat{\xi},\hat{\tau}) = 4\dot{\hat{\sigma}}G(\hat{\xi}) \Big/ \left(1-2\dot{\hat{\sigma}}\hat{y}_0\right)^{1/2}, \tag{4.30a}$$

$$u(\hat{\xi},\hat{\tau}) = -\left(1-2\dot{\hat{\sigma}}\hat{y}_0\right)^{1/2}/4G(\xi)\,, \qquad \xi = (1-2\dot{\hat{\sigma}}\hat{y}_0)\hat{\xi}\Big/4\dot{\hat{\sigma}}\,, \tag{4.30b}$$

with $G(\xi)$ given by (3.10). It is clear that (4.30) will become singular when $\dot{\hat{\sigma}}\hat{y}_0$ approaches $1/2$, the significance of which will become apparent shortly.

Using (3.11) and matching to (3.3) with $x_0 = \varepsilon^{-1/2}\mu\hat{Y}_0(\hat{\tau},\varepsilon)$ yields

$$\begin{aligned}&\frac{4\dot{\hat{\sigma}}B}{\left(1-2\dot{\hat{\sigma}}\hat{y}_0\right)^{1/2}}\exp\left[-\frac{1-2\dot{\hat{\sigma}}\hat{y}_0}{8\dot{\hat{\sigma}}}\hat{\xi}\right]\\ &\qquad\sim \mu\varepsilon^{1/2}\exp\left[1+\frac{\mu^2(\hat{Y}_0-\hat{y}_0)^2}{8}-\frac{\hat{Y}_0-\hat{y}_0}{4}\hat{\xi}\right].\end{aligned} \tag{4.31}$$

The comparison of (4.31) with (4.14) is instructive: the rim width $\hat{y}_0$ and the offset $\hat{Y}_0$ have become comparable. Requiring the algebraic terms in ε on the right-hand side of (4.31) to cancel requires $\hat{Y}_0 = \hat{y}_0 + 2$; (4.24) and the first of (4.25) are readily seen to be consistent with this in the limit of small $\hat{y}_0$. Comparison of the $\hat{\xi}$ terms then yields

$$\dot{\hat{\sigma}} = 1/2(\hat{y}_0+2), \tag{4.32}$$

thereby relating contact-line motion to rim thickness.

We are now in a position to return to the outer problem (4.27a), (4.28). While these PDEs are a familiar leading-order balance (see [13, 21, 27], for example), the BVP that follows is not the conventional one. Thus (4.28) is to be solved as a nonlocal BVP subject to

$$\hat{g} = 0 \text{ at } \hat{y} = 0 \text{ and at } \hat{y} = \hat{y}_0(\hat{\tau}), \tag{4.33}$$

$$\int_0^{\hat{y}_0(\hat{\tau})} \hat{g}(\hat{y},\hat{\tau})d\hat{y} = \hat{\sigma}(\hat{\tau}), \tag{4.34}$$

together with (4.32) and $\hat{\sigma}(\hat{\tau}) = 0$ at $\hat{\tau} = 0$. Once $\hat{g}$ and $\hat{\sigma}$ are determined in this way, $\hat{u}$ is given by integration of (4.27a) subject to $\hat{u} = 0$ and $\hat{\sigma}$ on $\hat{y} = 0$. We note that from (4.28), (4.33) we have that

$$\frac{\partial\hat{g}}{\partial\hat{y}} = -\left(1-2\dot{\hat{\sigma}}\hat{y}_0\right)^{1/2} \qquad \text{at } \hat{y} = \hat{y}_0. \tag{4.35}$$

Small and large $\hat{\tau}$. The small $\hat{\tau}$ limit of this BVP can be shown to match into the $\bar{\tau}\to\infty$ analysis of section 4.2, see (4.20)–(4.23), but we omit details. In the limit $\hat{\tau}\to\infty$, we obtain the more conventional zero-contact angle case because $\hat{y}_0\to\infty$ holds, leading from (4.32) to

$$\dot{\hat{\sigma}} \sim \frac{1}{2\hat{y}_0}, \tag{4.36}$$

and hence to the singular behavior noted above in connection with (4.30). In more detail, as $\hat{\tau} \to \infty$, the outer region itself splits into two, its own outer, $\hat{y} = \mathcal{O}(\hat{y}_0)$, being given by

$$\hat{g}(\hat{y}, \hat{\tau}) \sim \hat{y}_0 \Phi(\hat{\zeta}), \qquad \hat{\zeta} = \hat{y}/\hat{y}_0,$$

with

$$\Phi \frac{\partial^2 \Phi}{\partial \hat{\zeta}^2} - \frac{1}{2}\left(\frac{\partial \Phi}{\partial \hat{\zeta}}\right)^2 = \frac{1}{2}(\hat{\zeta} - 1), \tag{4.37a}$$

$$\Phi = 0 \quad \text{at} \quad \hat{\zeta} = 0 \quad \text{and at} \quad \hat{\zeta} = 1, \tag{4.37b}$$

so that, using (4.34) and (4.36),

$$\hat{\sigma}(\hat{\tau}) \sim \left(\frac{3\kappa\hat{\tau}}{4}\right)^{2/3}, \qquad \hat{y}_0(\hat{\tau}) \sim \left(\frac{3\hat{\tau}}{4\kappa^2}\right)^{1/3} \qquad \text{as } \tau \to \infty, \tag{4.38}$$

where the constant κ is given in terms of (4.37) by

$$\kappa = \left[\int_0^1 \Phi(\hat{\zeta}) d\hat{\zeta}\right]^{1/2}.$$

Using numerical results from [27], we obtain that $\kappa = 2\sqrt{M}$, with $M \approx 0.0272$, so that $\kappa \approx 0.330$. It follows from (4.37) that

$$\Phi(\hat{\zeta}) \sim \frac{2}{\sqrt{3}}\left(1 - \hat{\zeta}\right)^{3/2} \qquad \text{as } \hat{\zeta} \to 1^-. \tag{4.39}$$

By (4.27a), $\hat{u} = \mathcal{O}(\hat{\tau}^{-2/3})$ in this region: setting

$$\hat{g} \sim \hat{\tau}^{1/3}\hat{G}(\hat{\eta}), \quad \hat{u} \sim \hat{\tau}^{-2/3}\hat{V}(\hat{\eta}), \quad \hat{\eta} = \hat{y}/\hat{\tau}^{1/3},$$

wherein $\hat{G}$ and $\hat{\eta}$ are rescaled versions of Φ and $\hat{\zeta}$, implies that $\hat{V}$ is given by

$$\frac{1}{3}\left(\hat{G} - \hat{\eta}\frac{d\hat{G}}{d\hat{\eta}}\right) + \frac{d}{d\hat{\eta}}\left(\hat{G}\hat{V}\right) = 0,$$
$$\hat{V} = 0 \quad \text{at } \hat{\eta} = 0;$$

the mass flux $\hat{g}\hat{u}$ therefore scales as $\hat{\tau}^{-1/3}$.

The inner regime associated with the $\hat{\tau} \to \infty$ limit of the outer problem (4.27a), (4.28) exploits the $\hat{y}_0 \to \infty$ implication of (4.32) that

$$1 - 2\dot{\hat{\sigma}}\hat{y}_0 \sim 2/\hat{y}_0, \tag{4.40}$$

so by (4.35) the effective contact angle $\partial\hat{g}/\partial\hat{y}$ at $\hat{y} = \hat{y}_0$ scales with $\hat{\tau}^{-1/6}$. By (4.39), this in turn implies

$$1 - \hat{\zeta} = O(\hat{\tau}^{-1/3}), \quad \hat{y}_0 - \hat{y} = O(1), \quad \hat{g} = O(\hat{\tau}^{-1/6}), \quad \hat{u} = O(\hat{\tau}^{-1/6}),$$

and the scalings

$$\hat{y} = \hat{y}_0 + \hat{Z}, \qquad \hat{g} = \hat{y}_0^{-1/2}\hat{H}(\hat{Z}), \qquad \hat{u} = \hat{y}_0^{-1/2}\hat{U}(\hat{Z}) \tag{4.41}$$

give

$$\hat{H}\hat{U} = -\frac{1}{2}, \qquad \hat{H}\frac{\mathrm{d}^2\hat{H}}{\mathrm{d}\hat{Z}^2} - \frac{1}{2}\left(\frac{\mathrm{d}\hat{H}}{\mathrm{d}\hat{Z}}\right)^2 = -1 + \frac{1}{2}\hat{Z} \tag{4.42}$$

in $\hat{Z} < 0$, subject to

$$\hat{H} = 0, \quad \text{at } \hat{Z} = 0, \qquad \hat{H} \sim \frac{2}{\sqrt{3}}\left(-\hat{Z}\right)^{3/2} \qquad \text{as } \hat{Z} \to -\infty, \tag{4.43}$$

completing the description of the large $\hat{\tau}$ limit of the outer problem; that of the inner follows at once from the scaling laws (4.30).

An exact calculation from (4.31) is again revealing, giving

$$\hat{Y}_0 = 1/2\dot{\hat{\sigma}}, \tag{4.44a}$$

$$1 - 2\dot{\hat{\sigma}}\hat{y}_0 = 4\dot{\hat{\sigma}}\left(1 + \left(2\left(\ln\left(4B\dot{\hat{\sigma}}/\mu\right) - 1\right) - \ln\left(1 - 2\dot{\hat{\sigma}}\hat{y}_0\right)\right)/\mu^2\right)^{1/2}. \tag{4.44b}$$

5. A continuum of timescales between the third and fourth timescales. The important clue for what follows is (4.44b): if $\hat{y}_0$ is exponentially large with respect to μ^2, then it implies, bearing in mind (4.32) and (4.40),

$$1 - 2\dot{\hat{\sigma}}\hat{y}_0 \sim \frac{2}{\hat{y}_0}\left(1 - \frac{\ln \hat{y}_0}{\mu^2}\right)^{1/2}, \tag{5.1}$$

the $1/\mu^2$ term having been negligible in section 4.3. Since this result modifies only the $\hat{Z} = \mathcal{O}(1)$ region of that subsection (in particular, (4.38) remains valid), we can set

$$\ln \hat{y}_0 \sim \frac{1}{3}\ln \hat{\tau} \tag{5.2}$$

in (5.1). Defining

$$T = \ln \hat{\tau}/\ln(1/\varepsilon),$$

(5.1) becomes

$$1 - 2\dot{\hat{\sigma}}\hat{y}_0 \sim \frac{2}{\hat{y}_0}\left(1 - \frac{T}{3}\right)^{1/2}. \tag{5.3}$$

The results of this section apply for $0 < T < 3$ and hence for t scaling with the powers of ε between $\varepsilon^{-1/2}$ and $\varepsilon^{-7/2}$, corresponding to the continuum of scales noted in this section's heading.

The only resulting change to the analysis of section 4.3 results from the implications of (5.3) for the effective contact angle, whereby the second of (4.42) is modified: on suppressing the hats, we instead have

$$HU = -\frac{1}{2}, \qquad H\frac{\partial^2 H}{\partial Z^2} - \frac{1}{2}\left(\frac{\partial H}{\partial Z}\right)^2 = -\left(1 - \frac{T}{3}\right)^{1/2} + \frac{1}{2}Z; \tag{5.4}$$

now introducing hatted variables with different meanings from that above by defining

$$\begin{aligned} Z &= \left(1 - \frac{T}{3}\right)^{1/2}\hat{Z}, \\ H(Z,T) &= \left(1 - \frac{T}{3}\right)^{3/4}\hat{H}(\hat{Z}), \qquad U(Z,T) = \left(1 - \frac{T}{3}\right)^{-3/4}\hat{U}(\hat{Z}), \end{aligned} \tag{5.5}$$

we recover the BVP (4.42)–(4.43).

This in effect concludes the analysis of these intermediate timescales, the main implication of which is the evolution of the (small) effective contact angle at the leading edge of the rim implied by (5.4), whereby

$$\frac{\partial H}{\partial Z} = -2^{\frac{1}{2}} \left(1 - \frac{T}{3}\right)^{1/4}$$

at $Z = 0$.

However, to set things up for the analysis of the final, and for the current purposes most important, timescale—i.e., the fourth timescale—we need to examine some aspects in slightly more detail. A refined analysis of (4.44) is required in order to understand the behavior when T is close to 3. The scalings required to give a distinguished limit therein are

$$\hat{\tau} = \mu^{-3}\varepsilon^{-3}\hat{t}, \qquad 1 - 2\dot{\hat{\sigma}}\hat{y}_0 = \Omega/\mu\hat{y}_0 \tag{5.6}$$

(this defines Ω) so that $t = \varepsilon^{-7/2}\hat{t}$, the fourth timescale being given by $\hat{t} = \mathcal{O}(1)$. This leads using (5.2) to

$$\Omega \sim 2\left(\ln(1/\varepsilon) - \frac{1}{3}\ln\hat{\tau} - \ln\Omega\right)^{1/2}$$

and hence to

$$\Omega \sim 2\left(-\frac{1}{3}\ln\left(\Omega^3\hat{t}\right)\right)^{1/2};$$

as $\hat{t} \to 0$ we recover (5.3), so that

$$\Omega \sim 2\ln^{1/2}\left(1/\hat{t}\right)\Big/\sqrt{3} \tag{5.7}$$

captures the relevant aspects of the small $\hat{t}$ behavior of the fourth timescale, this analysis also serving to illustrate how (5.3) breaks down for $\hat{t} = \mathcal{O}(1)$.

Similar slight modifications to a number of scalings are needed when setting $\hat{t} = \mathcal{O}(1)$ within the current results: (4.44) implies using (4.36) that

$$\hat{Y}_0 \sim \hat{y}_0 + \Omega/\mu. \tag{5.8}$$

In (4.30)

$$\xi \sim \Omega\hat{\xi}/2\mu$$

holds, so that $\hat{\xi} = \mathcal{O}(\mu)$ and hence

$$\hat{y} = \hat{y}_0 + O(1/\mu) \tag{5.9}$$

holds both in the inner region associated with (4.30) and, because of (5.5), in that described by (5.4); moreover, in view of (5.8), $\hat{Y}_0 - \hat{y}_0$ scales in the same way, indicating the merging together of multiple regions and, in particular, (3.3) is no longer applicable.

We are now in a position to turn to our final timescale.

6. The fourth timescale. As implied by the preceding analysis, the appropriate timescale here is

$$t = \varepsilon^{-7/2}\breve{t} \tag{6.1}$$

(i.e., $\breve{t} = \hat{t}$, the change in notation being expedient here) so (4.38) implies the outer rescalings

$$\hat{y} = \breve{x}/\varepsilon\mu, \qquad \hat{y}_0(\hat{\tau}) = \breve{x}_0(\breve{t})/\varepsilon\mu, \qquad \hat{\sigma}(\hat{\tau}) = \breve{s}(\breve{t})/\varepsilon^2\mu^2,$$

i.e., in the original variables

$$x = \varepsilon^{-3/2}\breve{x}, \qquad s = \varepsilon^{-3}\breve{s},$$

while the scalings leading to (4.37) similarly imply

$$h = \varepsilon^{-3/2}\breve{h}, \qquad u = \varepsilon^2\breve{u}$$

to give at leading order a nonlocal problem in $0 < \breve{x} < \breve{x}_0(\breve{t})$, namely,

$$\frac{\partial \breve{h}}{\partial \breve{t}} + \frac{\partial}{\partial \breve{x}}\left(\breve{u}\breve{h}\right) = 0, \tag{6.2a}$$

$$\breve{h}\frac{\partial^2 \breve{h}}{\partial \breve{x}^2} - \frac{1}{2}\left(\frac{\partial \breve{h}}{\partial \breve{x}}\right)^2 = \dot{\breve{s}}\breve{x} - \frac{1}{2}, \tag{6.2b}$$

$$\breve{h} = 0, \quad \breve{u} = 0 \quad \text{at } \breve{x} = 0, \qquad \breve{h} = 0 \quad \text{at } \breve{x} = \breve{x}_0(\breve{t}),$$

$$\int_0^{\breve{x}_0} \breve{h}\, d\breve{x} = \breve{s}(\breve{t}), \qquad \dot{\breve{s}}\breve{x}_0 = 1/2, \qquad \breve{s}(0) = \breve{x}_0(0) = 0,$$

this IBVP determining $\breve{s}$ and $\breve{x}_0$ as well as $\breve{h}$ and $\breve{u}$ and implying that $\breve{u}\breve{h} = -\dot{\breve{s}}$ at $\breve{x} = \breve{x}_0(t)$. It is identical to that arising in the large $\hat{\tau}$ analysis of section 4.3, so that, in particular,

$$\breve{s}(\breve{t}) = \left(\frac{3\kappa\breve{t}}{4}\right)^{2/3}, \qquad \breve{x}_0(\breve{t}) = \left(\frac{3\breve{t}}{4\kappa^2}\right)^{1/3}; \tag{6.3}$$

see (4.38). We note here that these scaling laws for the contact-line location $\breve{s}$ and the rim width $\breve{x}_0$ are the ones found (for equivalent reasons) for the scalar slip-dominated/intermediate-slip thin-film model (i.e., with mobility h^2) in [13] and [27]. We make use of this later in section 8.

The arguments at the end of section 5 imply for the merged inner that the scalings

$$\breve{x} = \breve{x}_0(\breve{t}) + \varepsilon\breve{z}, \qquad \breve{h} = \varepsilon^{3/2}h, \qquad u = \varepsilon^{1/2}\breve{U}$$

hold, yielding at leading order the ODE system

$$\breve{U}h = -\dot{\breve{s}}, \qquad 4\frac{\partial}{\partial \breve{z}}\left(h\frac{\partial \breve{U}}{\partial \breve{z}}\right) + h\frac{\partial^3 h}{\partial \breve{z}^3} = \dot{\breve{s}} + \breve{U}. \tag{6.4}$$

The scaling properties of the above system imply

$$\breve{h}(\breve{x},\breve{t}) = \breve{t}^{1/3}\breve{f}(\breve{x}/\breve{t}^{1/3}), \qquad \breve{u}(\breve{x},\breve{t}) = \breve{t}^{-2/3}\breve{v}(\breve{x}/\breve{t}^{1/3}).$$

Since

$$\breve{h} \sim \left(\frac{8\dot{\breve{s}}}{3}\right)^{1/2} (\breve{x}_0 - \breve{x})^{3/2}, \qquad \breve{u} \sim -\left(\frac{3\dot{\breve{s}}}{8}\right)^{1/2} (\breve{x}_0 - \breve{x})^{-3/2} \qquad \text{as } \breve{x} \to \breve{x}_0^-$$

express the local behavior at the edge of the rim in the inner variables, (6.4) is subject to the matching conditions

$$\breve{h} \sim \left(\frac{8\dot{\breve{s}}}{3}\right)^{1/2} (-\breve{z})^{-3/2}, \qquad \breve{u} \sim -\left(\frac{3\dot{\breve{s}}}{8}\right)^{1/2} (-\breve{z})^{-3/2} \qquad \text{as } \breve{z} \to -\infty. \tag{6.5}$$

The system (6.4) is equivalent to

$$4\dot{\breve{s}}\frac{\partial}{\partial \breve{z}}\left(h\frac{\partial h}{\partial \breve{z}}\right) + h\frac{\partial^3 h}{\partial \breve{z}^3} = \dot{\breve{s}}\left(1 - \frac{1}{h}\right) \tag{6.6}$$

and a degree-of-freedom count on (6.5) (cf. [20]) shows that (6.5) constitutes a single boundary condition as $\breve{z} \to -\infty$. Given the $\breve{z}$-translation invariance of (6.4) only one boundary condition is needed as $\breve{z} \to +\infty$ and it is readily seen that

$$h \to 1 \qquad \text{as } \breve{z} \to +\infty \tag{6.7}$$

suppresses a single exponentially growing term, implying that (6.5), (6.7) specify the solution to (6.6) up to translations of $\breve{z}$. This far-field is worth elaborating upon further since it captures a qualitative transition that takes place on this timescale: Setting $h \sim 1 + \exp(-\lambda\breve{z})$ and linearizing for $\exp(-\lambda\breve{z}) \ll 1$ leads to

$$\lambda^3 - 4\dot{\breve{s}}\lambda^2 + \dot{\breve{s}} = 0. \tag{6.8}$$

For $\dot{\breve{s}}$ sufficiently large, corresponding to sufficiently small $\breve{t}$, (6.8) has three real roots, one negative, which must be suppressed, and two positive. For $\dot{\breve{s}}$ sufficiently small, that is, $\breve{t}$ sufficiently large, there is one negative real root and a complex-conjugate pair with positive real part. The transition between the two occurs at the repeated-root value

$$\lambda = 3\dot{\breve{s}}/8, \qquad \dot{\breve{s}} = (27)^{1/2}/16$$

and the corresponding value of $\breve{t}$ can then be obtained from (6.3). Thus one has a rather precise criterion for the transition from monotonic decay at the leading edge of the rim for smaller values of $\breve{t}$ to oscillatory decay (with an infinite sequence of oscillations) for larger $\breve{t}$. This type of profile is indicated in the initial schematic, Figure 1(b).

7. Summary. Here we summarize the balances that hold on the various time scales and highlight some of the key features. In this section, we adopt the notation $H(\eta)$, $U(\eta)$, S (where S is a constant) for all similarity solutions: these differ in form in each case, but $\eta = \mathcal{O}(1)$ characterizes the width of the rim. Further quantities of interest are the gap between $y = y_0$, the leading edge of the thickening rim, and $y = Y_0$, about which the rapid drop-off to the initial film thickness $h = 1$ occurs, together with the effective contact angle at $y = y_0$.

7.1. Second and third timescales. Equations (4.4a) and (4.5) govern the behavior to all orders in $1/\mu$, and the subdivision into two distinct timescales generates leading-order solutions that are only logarithmically accurate with respect to ε. On the second timescale (4.7) governs the outer behavior, substrate friction entering only implicitly via the far-field (matching) condition (4.16). The time dependence of the large $\bar{\tau}$ behavior can be expressed in the form

$$h \sim t^{1/2} H(\eta), \quad u \sim t^{-1/2} U(\eta), \quad s \sim St, \quad \eta = x/t^{1/2}, \tag{7.1}$$

wherein H adopts a parabolic—and hence symmetric—profile. On this timescale, the rim is diffuse in the sense that its thickness drops off exponentially, as in (4.10), rather than the asymptotics leading to a sharp-interface limit, though one such is manifest as $\bar{\tau} \to \infty$, as in (4.20), for which the symmetry of the rim profile implies that the effective contact angle at the leading edge of the rim coincides with the imposed one at the trailing edge. On the third timescale substrate friction makes itself felt in the outer region—see (4.28), which is coupled to (4.27a). The nonlocal nature of the problem that determines the rim profile over this timescale is worth highlighting. Its large $\hat{\tau}$ behavior (see (4.38)) is associated with the time dependence

$$h \sim t^{1/3} H(\eta), \quad u \sim t^{-2/3} U(\eta), \quad s \sim St^{2/3}, \quad \eta = x/t^{1/3}. \tag{7.2}$$

The spacing $\hat{Y}_0 - \hat{y}_0$ alluded to above is fixed at two over this timescale and the leading-edge contact angle is given by (4.35): since

$$1 - 2\dot{\hat{\sigma}}\hat{y}_0 = 4\dot{\hat{\sigma}}$$

over this timescale, which scales at $t^{-1/6}$ as $\hat{\tau} \to \infty$, the leading-order similarity solution has zero contact angle at the leading edge.

7.2. Transition timescales. Over the timescales described in section 5, (7.2) is entirely unaltered, but now

$$\hat{Y}_0 - \hat{y}_0 \sim 2(1 - \tau/3)^{1/2}$$

and (4.35) is replaced by

$$\frac{\partial \hat{g}}{\partial \hat{y}} \sim -2\dot{\hat{\sigma}}^{1/2} (1 - \tau/3)^{1/4} \qquad \text{at} \quad \hat{y} = \hat{y}_0$$

indicating a further drop-off in the effective contact angle at the leading edge of the rim.

7.3. Fourth timescale. From the large $\bar{\tau}$ behavior on the second timescale onward, the first term in (2.1b) is negligible in the governing PDEs in the outer region, so the dominant balance in (2.1) is simply

$$\frac{\partial h}{\partial t} - \dot{s}\frac{\partial h}{\partial x} + \frac{1}{\varepsilon}\frac{\partial}{\partial x}\left(h^2 \frac{\partial^3 h}{\partial x^3}\right) = 0 \tag{7.3}$$

or a limit case thereof—in other words one has (in a convected frame of reference) a very familiar thin-film equation. Nevertheless, on the second and third timescales the first term in (2.1b) does have an important effect through the leading-edge contact-angle condition on the rim—see (4.35), in particular—and many of the subtleties of the above analysis are associated with this nontrivial matching. However, by the $\hat{\tau} \to \infty$

limit of the third timescale, the rim has become so deep that the effective contact angle becomes negligible, so that over the fourth timescale we are in territory familiar from the analysis of (7.3). However, the inner analysis there—see (6.6)—does include otherwise-neglected terms and yields additional insights into the transition between monotonic and oscillatory decay that is experimentally observable.

8. Comparison with numerical solutions. The systematic asymptotic analysis has revealed a rich behavior of the solution which can be compared to numerical results. We will focus here on two features. Since we have identified power laws or near power laws as leading-order approximations of the evolution of the contact line $s(t)$ in various time regimes, our first, semiquantitative comparison will center on identifying the exponents of this behavior in the numerical results. For the second comparison, we look at the transition from monotonic decay at the leading edge of the rim to oscillatory decay described at the end of section 6.

Regarding the first point, we first illustrate the general behavior of the contact line by presenting numerical results for $s(t)$ in Figure 2 for three different values of ε; details of the finite-difference discretization method are given in Appendix A. We notice that $s(t)$ increases faster for the smaller ε, as one may expect since this represents larger slip. Taking into account the log-log scaling of the axes, the difference is quite dramatic and leads to a rapid growth of the rim for the smaller values of ε. Moreover, all three lines are not straight, signaling a departure from a single power-law behavior as predicted by the asymptotics. To quantify this change, we note that

$$\rho(t) \equiv \frac{d\ln s}{d\ln t} = \frac{t}{s}\frac{ds}{dt} \tag{8.1}$$

can be used to extract the exponent of an approximate power-law behavior of $s(t)$. If, for instance, $s(t) \sim \eta(t)t^r$ for $t \to \infty$, with constant r and a prefactor η that varies more slowly in t than any power law (logarithmic factors do not change ρ to leading order), then (8.1) gives $\rho(t) \sim r$. Moreover, if s follows a power-law behavior in a

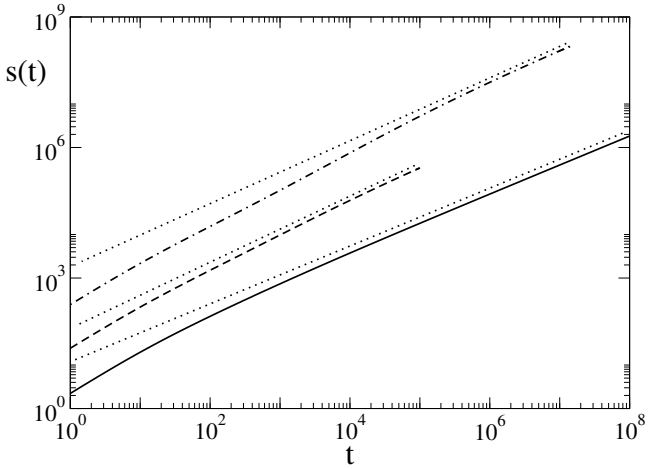

FIG. 2. *The evolution of the contact line $s(t)$, obtained from numerical solutions for the profile and contact-line evolution. Shown are the results for three values of $\varepsilon = 0.01$, 10^{-4}, and 10^{-6} by the solid, dashed, and dot-dashed curves, respectively. The thin dotted straight lines are included as a visual aid to make it easier to see that these curves are not straight.*

TABLE 1

Overview of the time regimes, grouped by the typical behavior of the contact-line evolution $s(t)$ as represented by the exponent $\rho(t)$ defined in (8.1). *The table shows the lower and upper asymptotic bounds for each regime. Further explanations are given in the text.*

Regime	Lower bound	Upper bound	Contact-line behavior
A	–	1	Determined by initial condition
B	1	$\varepsilon^{-1/2}\ln^{3/2}(1/\varepsilon)$	ρ approaches 1
C	$\varepsilon^{-1/2}\ln^{3/2}(1/\varepsilon)$	$\varepsilon^{-7/2}$	ρ approaches 2/3
D	$\varepsilon^{-7/2}$	–	$\rho(t) \sim 2/3$

particular time regime when $\varepsilon \to 0$, then ρ converges to the corresponding exponent in this regime.

The asymptotic results predict up to four distinctive regimes for $\rho(t)$, summarized in Table 1: an initial regime A, t up to $\mathcal{O}(1)$, where the solution is determined by the inital condition, followed by the regime B between the first and third timescales, $1 \ll t \ll \varepsilon^{-1/2}\ln^{3/2}(1/\varepsilon)$, where $\rho(t)$ approaches 1. After that, we have the regime C, $t = \mathcal{O}(\varepsilon^{-1/2}\ln^{3/2}(1/\varepsilon))$ up to $t \ll \varepsilon^{-7/2}$, i.e., from the third to the fourth timescale, where the trend is reversed so that ρ begins to decrease until it approaches 2/3, where it stays for the final regime D, $t = \mathcal{O}(\varepsilon^{-7/2})$, i.e., for times of the order of the fourth timescale, and beyond. While the exponent ρ does not change to leading order in the final regime, the downstream part transitions to a profile with an infinite train of capillary waves. This feature will be investigated further below.

The numerical results for ρ are shown in Figure 3(a) for three different values of ε. For the two smaller values, one clearly sees that, after an initial descending transient, ρ indeed increases, indicating that we have entered regime B. To get a more precise estimate for the validity of (4.1), and hence for the onset of the increase, recall that (4.1) is the approximate solution of (4.2), which, in fact, assumes that $\ln(t/8) \gg 1$. A value of $t = 200$ gives $\ln(t/8) \approx \sqrt{10}$, which we take as a suitable minimum for (4.1) to be valid. This value is shown in Figure 3(a) as a dotted vertical line, and it is indeed near where the graphs for ρ for the two smaller values of ε have a minimum.

On the other hand, the solid bullets mark, for each of the curves, the times $t = \varepsilon^{-1/2}\ln^{3/2}(1/\varepsilon)$, to indicate the lower bound of regime C in which we expect the trend of ρ to be reversed. Indeed, for all three curves, the bullet lies in a region where the graphs are monotonically decreasing. Moreover, for $\varepsilon = 10^{-2}$, the bullet lies left of 200 so that the transition to regime C occurs before regime B can fully develop. This explains why a region with an increase of ρ is only visible in the graphs for the two smaller ε.

We now focus on the regime D and the appearance of capillary waves at $x \to \infty$, i.e., where the rim profile h decays toward a flat film of thickness 1, as indicated in the schematic in Figure 1(b). This regime is characterized by the timescale $t = \varepsilon^{-7/2}$, which is large and difficult to access numerically, so we only followed our numerical simulations up to this regime for the largest of our three values of $\varepsilon = 10^{-2}$, so that $\varepsilon^{-7/2} = 10^7$. The transition to a rim profile with an oscillatory decay has been observed previously for a thin-film model with an intermolecular potential [27] and in experiments [2], but now we can give an analytical expression for the time t^{trans} when this transition occurs.

We first note that the train of capillary waves appears when $\dot{\breve{s}}$ passes the value where the roots of (6.8) become complex conjugate. This value was determined in the previous section to be $\dot{\breve{s}} = \sqrt{27}/16$. Using the derivative of the first expression

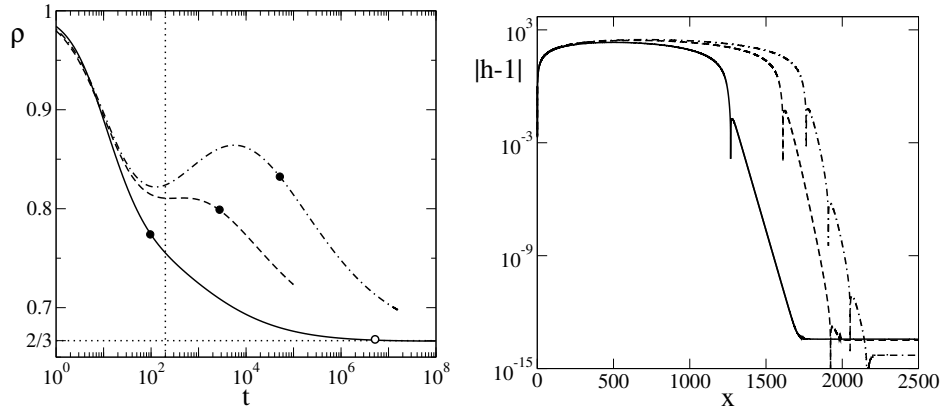

FIG. 3. (a) *The evolution of the exponent $\rho(t)$ as defined in* (8.1)*, obtained from numerical solutions for the profile and contact-line evolution. Shown are the results for three values of $\varepsilon = 0.01$, 10^{-4}, and 10^{-6} by the solid, dashed, and dot-dashed curves, respectively. The vertical dotted line and the symbols are explained in the text.* (b) *Profiles for $h-1$ for $\varepsilon = 0.01$ at times $t = 0.275\times10^7$, $t = 0.575\times10^7$, and $t = 0.759\times10^7$ in a semilog plot, shown by solid, dashed, and dash-dotted lines, respectively.*

in (6.3) to approximate $\dot{\breve{s}}(\breve{t})$, we can estimate the corresponding $\breve{t}^{\text{trans}}$ and then scale back to obtain t^{trans}. The constant κ which appears in (6.3) needs to be determined numerically by solving (4.37). Hence, using the previously stated value for $\kappa \approx 0.330$, we obtain

$$\breve{t}^{\text{trans}} = \frac{2^{11}}{3^{11/2}}\kappa^2 = 0.529, \tag{8.2}$$

that is, $t^{\text{trans}} = 0.529\,\varepsilon^{-7/2}$. In Figure 3(a), this value is shown only for $\varepsilon = 0.01$, it being indicated by an open circle (placed at $t = 0.529\times10^7$).

The behavior of the numerically obtained rim profiles is best seen in a semilog plot of $|h-1|$. Whenever $h-1$ passes through zero, the plot of $|h-1|$ produces a readily observable "spike." A superposition of two exponentials $\exp(-\lambda\breve{z})$ in the linearization of $h-1$ with two real values for λ only allows for at most one zero at finite values of $\breve{z}$; two and more zeros arise if, and only if, there is a conjugate complex pair of λ's and hence indicate the transition to a profile with a train of decaying capillary waves (which would have infinitely many oscillations on an infinite domain). It is clearly seen that the left, solid curve for $t = 0.275\times10^7$ has only one spike, while the dash-dotted one, which is for $t = 0.759\times10^7$, has three. For $t = 0.575\times10^7$, we see a second spike close to the cut-off provided by the accuracy of our numerical calculations. This time is very close to the value predicted for t^{trans}.

9. Summary and conclusion. For a model of a dewetting liquid with strong slip, characterized by small ε, we have analyzed the evolution of the film and contact line asymptotically. The problem shows a rich behavior as $\varepsilon \to 0$, passing through several time regimes. Two predictions from the asymptotics regarding the exponents of an approximation by a power-law type behavior and the transition from a monotonically decaying profile to one with a train of decaying capillary waves could be identified in numerical solutions.

To see that all the regimes of the rim evolution occur for a single set of parameters and initial data and, in particular, first see an increase of ρ toward 1 (in regime B) and then convergence to a 2/3 law (in regime C), one needs to use very large slip

lengths—that is, $\varepsilon < 10^{-4}$—and observe the evolution up to dimensionless times on the order of 10^6 before $\rho(t)$ is less than, say, 0.7. By this time, the height of the rim has already grown by a factor of about 1000. In typical physical experiments, only factors on the order 10s are achieved [2] at best, so the observation of both trends for ρ in a single experiment seems elusive. However, individual phases of the evolution are within reach. The transition from a profile with a monotonically decaying to an oscillatory tail has been observed in experiments with dewetting polystyrene films [2] for large, but not too large, β. The slip length in these experiments is on the order of 10 compared to the thickness of the unperturbed film, and with typical slopes on the profile facing the undisturbed rim not being small, about 0.4 (which is, in fact, at the margin of where a thin film theory is valid), ε is not too much larger than 1 and the transition to an oscillatory profile happens within the limitations of the experiment. In contrast, observations of a nonmonotonic behavior of the power-law exponent ρ, as seen for the dashed and dot-dashed curves in Figure 3(a), require a value for ε of 10^{-3} or less, meaning slip lengths more than 10000 times the thickness of the originally deposited film. This is beyond the values that can be obtained in typical experiments [9, 10].

Several extensions would be interesting. The first is to extend the analysis to the case where the contact angle is not small. Moderate contact angles are of practical interest, since liquid film dewetting with strong slip has been typically observed in experiments with very hydrophobic liquid/solid combination, where contact angles are in the range of 67° or more [9, 10, 11]. This means that a thin-film approximation is no longer uniformly valid, so that the full fluid-mechanical equations need to be used in some of the spatial and temporal regimes. A practical, albeit asymptotically slightly inconsistent, approach that has been frequently used for free suspended films that rupture is to apply the thin-film approximation in the bulk but retain the full nonlinear curvature in the expression for the surface tension [14, 5].

For long chain lengths, polymer liquids also tend to exhibit non-Newtonian flow properties, in particular viscoelastic behavior [33], which can be easily included in a strong-slip model [4]. Also, while the model in this paper does not explicitly incorporate intramolecular forces via a conjoining/disjoining pressure, they are easily included in a thin film model [27]. Their effect is important where rupture phenomena are studied either through spinodal decomposition of a flat film [16, 30] or as satellite hole formation through secondary rupture events induced by the capillary waves preceding a dewetting rim [3].

An aspect that is also straightforward to incorporate in the strong-slip model is the presence of inertia [27]. This would become relevant in situations where the slip length becomes very large and the film-profile evolution approaches that of a suspended film where no substrate is present. The evolution of suspended thin films as they arise from bursting bubbles or, for a different geometry, from retracting jets has been extensively studied, e.g., in [35, 14, 18, 34, 37, 38, 6, 17] and references therein. For a planar suspended film that is symmetric with respect to its mid-plane, there are no tangential stresses along this plane, corresponding to a substrate with an infinite slip length, i.e., $\varepsilon = 0$. It remains to be seen if range of very large slip lengths can be realized in experiments, but from a mathematical point of view, a discussion of regimes where both inertial and slip effects are significant would be interesting but also challenging.

Appendix A. Numerical method. For the numerical discretization of (2.1)–(2.2), we first truncate the semi-infinite spatial domain at $x = L$, where $L > 0$ is chosen to be large enough so that effect of the growing rim on the unperturbed film

near $x = L$ is negligibly small over the time period for which the simulation is carried out. At $x = L$, we impose

$$h = 1, \qquad u = -\dot{s}. \tag{A.1}$$

We then use a staggered grid approximation by first introducing an equidistant grid with nodes $x_i = i\Delta x$, $i = 0 \dots N$, $\Delta x = L/N$, and then approximating $h(x_i) \approx h_i$ and $u(x_{i+1/2}) \approx u_{i+1/2}$. The PDEs are discretized by central finite differences in space and an implicit Euler step in time (with step size Δt) so that

(A.2)
$$\frac{h_i^+ - h_i}{\Delta t} + \frac{1}{\Delta x}\left[\frac{h_{i+1}^+ + h_i^+}{2}u_{i+1/2}^+ - \frac{h_i^+ + h_{i-1}^+}{2}u_{i-1/2}^+\right] = 0, \quad i = 1, \dots, N-1,$$

$$\frac{h_{i+1}^+ + h_i^+}{2}\frac{h_{i+2}^+ - 3h_{i+1}^+ + 3h_i^+ - h_{i-1}^+}{(\Delta x)^3} + 4\frac{v_{i+1}^+ - v_i^+}{\Delta x} = \varepsilon\left(u_{i+1/2}^+ + \frac{s^+ - s}{\Delta t}\right),$$

$$i = 0, \dots, N-1. \tag{A.3}$$

The superscript + indicates grid values taken on the new time level, and v_i are given by

$$v_0^+ = 0, \qquad v_N^+ = 0, \tag{A.4}$$

$$v_i^+ = h_i^+\frac{u_{i+1/2}^+ - u_{i-1/2}^+}{\Delta x}, \qquad i = 1, \dots, N-1, \tag{A.5}$$

and we set

$$h_0^+ = 0, \qquad h_{-1}^+ = h_1^+ - 2\Delta x, \tag{A.6}$$

$$h_{N-1}^+ = h_{N+1}^+, \qquad u_{N-1/2}^+ = -\frac{s^+ - s}{\Delta t}. \tag{A.7}$$

The equations in (A.6) result from the discretization of the first two boundary conditions in (2.2a), and the ones in (A.7) result from (A.1). Near $x = L$, u becomes spatially uniform, so hu_x vanishes, justifying the second of the two conditions in (A.4). To argue for the first, notice that by combining (2.1a) and (2.2a) one gets $0 = h_t + (uh)_x = hu_x$ at $x = 0$.

Instead of enforcing $u = 0$ at $x = 0$ from (2.2a) for the final equation, we use global mass conservation, which can obtained from (2.1) and (2.2) via integration by parts, and discretize the relation via the trapezoidal rule, to get

$$\sum_{i=0}^{N-1}\frac{h_i^+ + h_{i+1}^+}{2}\Delta x - \sum_{i=0}^{N-1}\frac{h_i^0 + h_{i+1}^0}{2}\Delta x = s_+. \tag{A.8}$$

Here, h_i^0 denotes the value of the initial condition for h at the ith grid point. The nonlinear set of equations is solved using Newton's method, and step doubling is used to estimate the error and adjust the step sizes.

Appendix B. Nonlocal transformations. This appendix is included largely to record connections between the system (2.1) and PDEs that have arisen in other contexts. In view of (2.6), m can (as usual) be interpreted as a Lagrangian variable, whereby

$$u = \frac{\partial x}{\partial t}(m, t)$$

and, under the hodograph transformation, (2.7) is equivalent to

$$\frac{4}{(\partial x/\partial m)}\frac{\partial}{\partial m}\left(\frac{1}{(\partial x/\partial m)^2}\frac{\partial^2 x}{\partial m \partial t}\right) - \frac{1}{(\partial x/\partial m)^2}\frac{\partial}{\partial m}\left(\frac{1}{(\partial x/\partial m)}\frac{\partial}{\partial m}\left(\frac{1}{(\partial x/\partial m)^3}\frac{\partial^2 x}{\partial m^2}\right)\right) = \varepsilon\left(\dot{s} + \frac{\partial x}{\partial t}\right).$$

Hence

$$\varepsilon\frac{\partial \sigma}{\partial t} = 4\frac{\partial}{\partial m}\left(\frac{1}{\sigma}\frac{\partial}{\partial m}\left(\frac{1}{\sigma^2}\frac{\partial \sigma}{\partial t}\right)\right) - \frac{\partial}{\partial m}\left(\frac{1}{\sigma^2}\frac{\partial}{\partial m}\left(\frac{1}{\sigma}\frac{\partial}{\partial m}\left(\frac{1}{\sigma^3}\frac{\partial \sigma}{\partial m}\right)\right)\right), \tag{B.1}$$

where $\sigma = \partial x/\partial m = 1/h$. Note that σ in this section has a different meaning from elsewhere in the paper. Equation (B.1) is a highly nonlinear high-order scalar pseudoparabolic equation and various balances within it are instructive. That between the first and last terms is a special case of one of the classes analyzed in [19], and the analysis therein implies that (B.1) can be written in the alternative form

$$\varepsilon\frac{\partial \sigma}{\partial t} = \frac{\partial}{\partial m}\left(\frac{1}{\sigma}\frac{\partial}{\partial m}\left(\frac{4}{\sigma^2}\frac{\partial \sigma}{\partial t} - \frac{1}{\sigma^{5/2}}\frac{\partial}{\partial m}\left(\frac{1}{\sigma^{5/2}}\frac{\partial \sigma}{\partial m}\right)\right)\right). \tag{B.2}$$

The version (B.2) is particularly instructive when the left-hand side can be neglected; since

$$4h\frac{\partial u}{\partial x} + h\frac{\partial^2 h}{\partial x^2} - \frac{1}{2}\left(\frac{\partial h}{\partial x}\right)^2 = \frac{4}{\sigma^2}\frac{\partial \sigma}{\partial t} - \frac{1}{\sigma^{5/2}}\frac{\partial}{\partial m}\left(\frac{1}{\sigma^{5/2}}\frac{\partial \sigma}{\partial m}\right)$$

and (2.2a) implies on neglecting the right-hand side of (2.1b) that

$$4h\frac{\partial u}{\partial x} + h\frac{\partial^2 h}{\partial x^2} - \frac{1}{2}\left(\frac{\partial h}{\partial x}\right)^2 = -\frac{1}{2}, \tag{B.3}$$

the corresponding simplification of (B.2) is the reaction-diffusion equation

$$\frac{\partial \sigma}{\partial t} = \frac{1}{4\sigma^{1/2}}\frac{\partial}{\partial m}\left(\frac{1}{\sigma^{5/2}}\frac{\partial \sigma}{\partial m}\right) - \frac{\sigma^2}{8}, \tag{B.4}$$

i.e., introducing $\omega = \sigma^{3/2}$,

$$\frac{\partial \omega}{\partial t} = \frac{1}{4}\frac{\partial}{\partial m}\left(\omega^{-2}\frac{\partial \omega}{\partial m}\right) - \frac{3}{16}\omega^{5/3}. \tag{B.5}$$

Equation (B.5) is explicitly solvable when either of the terms on the right-hand side is negligible—this is obvious when the first is neglected; when the second can be, we have a nonlinear diffusion equation that is well-known to be transformable to the heat equation: integrating via $\omega = \partial w/\partial m$ and performing a further hodograph transformation gives, without loss of generality,

$$\frac{\partial m}{\partial t} = \frac{\partial^2 m}{\partial w^2}.$$

More generally, the reduction of the original fourth-order system to the second-order equation (B.4) is a significant one, though we shall make little use of it here. One reduction of order is achieved via the first integral (B.3) that holds on neglecting the

right-hand side of (2.1b). The second follows because the relevant equation allowing $h(x,t)$, $u(x,t)$ to be reconstructed from $\sigma(m,t)$, namely, the first-order ODE

$$\frac{\partial x}{\partial m} = \sigma,$$

decouples from (B.4); the remaining relationships

$$u = \frac{\partial x}{\partial t}, \qquad h = 1/\sigma,$$

require no integrations.

REFERENCES

[1] O. Bäumchen, R. Fetzer, A. Münch, B. Wagner, and K. Jacobs, *Comprehensive analysis of dewetting profiles to quantify hydrodynamic slip*, in IUTAM Symposium on Advances in Micro- and Nanofluidics, M. Ellero, X. Hu, J. Fröhlich, and N. Adams, eds., IUTAM Bookser. 15, Springer, Dordrecht, 2009, pp. 51–65.

[2] O. Bäumchen, L. Marquant, R. Blossey, A. Münch, B. Wagner, and K. Jacobs, *Influence of slip on the Rayleigh-Plateau rim instability in dewetting viscous films*, Phys. Rev. Lett., 113 (2014), 014501.

[3] J. Becker, G. Grün, R. Seemann, H. Mantz, K. Jacobs, K. R. Mecke, and R. Blossey, *Complex dewetting scenarios captured by thin-film models*, Nature Materials, 2 (2003), pp. 59–63.

[4] R. Blossey, A. Münch, M. Rauscher, and B. Wagner, *Slip vs. viscoelasticity in dewetting thin films*, Eur. Phys. J. E, 20 (2006), pp. 267–271.

[5] M. P. Brenner and D. Gueyffier, *On the bursting of viscous films*, Phys. Fluids, 11 (1999), pp. 737–739.

[6] F. E. C. Culick, *Comments on a ruptured soap film*, J. Appl. Phys., 31 (1960), pp. 1128–1129.

[7] T. Erneux and S. H. Davis, *Nonlinear rupture of free films*, Phys. Fluids A, 5 (1993), pp. 1117–1122.

[8] P. L. Evans, J. R. King, and A. Münch, *Intermediate-asymptotic structure of a dewetting rim with strong slip*, Appl. Math. Res. Express. AMRX, 2006 (2006), 25262.

[9] R. Fetzer, K. Jacobs, A. Münch, B. Wagner, and T. P. Witelski, *New slip regimes and the shape of dewetting thin liquid films*, Phys. Rev. Lett., 95 (2005), 127801.

[10] R. Fetzer, A. Münch, B. Wagner, M. Rauscher, and K. Jacobs, *Quantifying hydrodynamic slip: A comprehensive analysis of dewetting profiles*, Langmuir, 23 (2007), pp. 10559–10566.

[11] R. Fetzer, M. Rauscher, A. Münch, B. A. Wagner, and K. Jacobs, *Slip-controlled thin-film dynamics*, Europhys. Lett., 75 (2006), pp. 638–644.

[12] J. C. Flitton, *Inertia Dominated Spreading of Thin Films*, Ph.D. thesis, University of Nottingham, UK, 2001.

[13] J. C. Flitton and J. R. King, *Surface-tension-driven dewetting of Newtonian and power-law fluids*, J. Engrg. Math., 50 (2004), pp. 241–266.

[14] L. Gordillo, G. Agbaglah, L. Duchemin, and C. Josserand, *Asymptotic behavior of a retracting two-dimensional fluid sheet*, Phys. Fluids, 23 (2011), 122101.

[15] K. Jacobs, R. Seemann, G. Schatz, and S. Herminghaus, *Growth of holes in liquid films with partial slippage*, Langmuir, 14 (1998), pp. 4961–4963.

[16] K. Kargupta, A. Sharma, and R. Khanna, *Instability, dynamics, and morphology of thin slipping films*, Langmuir, 20 (2004), pp. 244–253.

[17] J. B. Keller, *Breaking of liquid films and threads*, Phys. Fluids, 26 (1983), pp. 3451–3453.

[18] J. B. Keller and M. J. Miksis, *Surface tension driven flows*, SIAM J. Appl. Math., 43 (1983), pp. 268–277.

[19] J. R. King, *Two generalisations of the thin film equation*, Math. Comput. Model., 34 (2001), pp. 737–756.

[20] J. R. King and M. Bowen, *Moving boundary problems and non-uniqueness for the thin film equation*, European J. Appl. Math., 12 (2001), pp. 321–356.

[21] J. R. King, A. Münch, and B. A. Wagner, *Linear stability analysis of a sharp-interface model for dewetting thin films*, J. Engrg. Math., 63 (2008), pp. 177–195.

[22] J. R. King and J. M. Oliver, *Thin-film modelling of poroviscous free surface flows*, European J. Appl. Math., 16 (2005), pp. 519–553.

[23] E. Lauga, M. Brenner, and H. Stone, *Microfluidics: The no-slip boundary condition*, in Springer Handbook of Experimental Fluid Mechanics, C. Tropea, A. Yarin, and J. Foss, eds., Springer, Berlin, 2007, pp. 1219–1240.
[24] A. Münch, *Dewetting rates of thin liquid films*, J. Phys. Condensed Matter, 17 (2005), pp. S309–S318.
[25] A. Münch and B. Wagner, *Contact-line instability of dewetting thin films*, Phys. D, 209 (2005), pp. 178–190.
[26] A. Münch, B. Wagner, M. Rauscher, and R. Blossey, *A thin-film model for corotational Jeffreys fluids under strong slip*, Eur. Phys. J. E, 20 (2006), pp. 365–368.
[27] A. Münch, B. A. Wagner, and T. P. Witelski, *Lubrication models with small to large slip lengths*, J. Engrg. Math., 53 (2006), pp. 359–383.
[28] D. Peschka, A. Münch, and B. Niethammer, *Self-similar rupture of viscous thin films in the strong-slip regime*, Nonlinearity, 23 (2010), pp. 409–427.
[29] D. Peschka, A. Münch, and B. Niethammer, *Thin-film rupture for large slip*, J. Engrg. Math., 66 (2010), pp. 33–51.
[30] M. Rauscher, R. Blossey, A. Münch, and B. Wagner, *Spinodal dewetting of thin films with large interfacial slip: Implications from the dispersion relation*, Langmuir, 24 (2008), pp. 12290–12294.
[31] C. Redon, F. Brochard-Wyart, and F. Rondelez, *Dynamics of dewetting*, Phys. Rev. Lett., 66 (1991), pp. 715–718.
[32] C. Redon, J. B. Brzoska, and F. Brochard-Wyart, *Dewetting and slippage of microscopic polymer films*, Macromolecules, 27 (1994), pp. 468–471.
[33] G. Reiter, M. Sferrazza, and P. Damman, *Dewetting of thin polymer films at temperatures close to the glass transition*, Eur. Phys. J. E, 12 (2003), pp. 133–138.
[34] V. Roisman, I, *On the instability of a free viscous rim*, J. Fluid Mech., 661 (2010), pp. 206–228.
[35] N. Savva and J. W. M. Bush, *Viscous sheet retraction*, J. Fluid Mech., 626 (2009), pp. 211–240.
[36] R. Seemann, S. Herminghaus, and K. Jacobs, *Shape of a liquid front upon dewetting*, Phys. Rev. Lett., 87 (2001), 196101.
[37] G. Sünderhauf, H. Raszillier, and F. Durst, *The retraction of the edge of a planar liquid sheet*, Phys. Fluids, 14 (2002), pp. 198–208.
[38] G. Taylor, *The dynamics of thin sheets of fluid. III. Disintegration of fluid sheets*, Proc. A, 253 (1959), pp. 313–321.
[39] T. Vilmin and E. Raphaël, *Dewetting of thin viscoelastic polymer films on slippery substrates*, Europhys. Lett., 72 (2005), pp. 781–787.